



# Patient-Specific Identification of Atrial Flutter Vulnerability—A Computational Approach to Reveal Latent Reentry Pathways

Axel Loewe<sup>1\*</sup>, Emanuel Poremba<sup>1</sup>, Tobias Oesterlein<sup>1</sup>, Armin Luik<sup>2</sup>, Claus Schmitt<sup>2</sup>, Gunnar Seemann<sup>1,3,4</sup> and Olaf Dössel<sup>1</sup>

<sup>1</sup> Institute of Biomedical Engineering, Karlsruhe Institute of Technology (KIT), Karlsruhe, Germany, <sup>2</sup> Medizinische Klinik IV, Städtisches Klinikum Karlsruhe, Karlsruhe, Germany, <sup>3</sup> Institute for Experimental Cardiovascular Medicine, University Heart Center Freiburg Bad Krozingen, Freiburg, Germany, <sup>4</sup> Faculty of Medicine, Albert-Ludwigs University, Freiburg, Germany

## OPEN ACCESS

### Edited by:

Patrick M. Boyle,  
University of Washington,  
United States

### Reviewed by:

Jichao Zhao,  
The University of Auckland,  
New Zealand  
Jason D. Bayer,  
Université de Bordeaux, France

### \*Correspondence:

Axel Loewe  
publications@ibt.kit.edu

### Specialty section:

This article was submitted to  
Computational Physiology and  
Medicine,  
a section of the journal  
Frontiers in Physiology

**Received:** 15 September 2018

**Accepted:** 18 December 2018

**Published:** 14 January 2019

### Citation:

Loewe A, Poremba E, Oesterlein T, Luik A, Schmitt C, Seemann G and Dössel O (2019) Patient-Specific Identification of Atrial Flutter Vulnerability—A Computational Approach to Reveal Latent Reentry Pathways. *Front. Physiol.* 9:1910. doi: 10.3389/fphys.2018.01910

Atypical atrial flutter (AFlut) is a reentrant arrhythmia which patients frequently develop after ablation for atrial fibrillation (AF). Indeed, substrate modifications during AF ablation can increase the likelihood to develop AFlut and it is clinically not feasible to reliably and sensitively test if a patient is vulnerable to AFlut. Here, we present a novel method based on personalized computational models to identify pathways along which AFlut can be sustained in an individual patient. We build a personalized model of atrial excitation propagation considering the anatomy as well as the spatial distribution of anisotropic conduction velocity and repolarization characteristics based on a combination of a priori knowledge on the population level and information derived from measurements performed in the individual patient. The fast marching scheme is employed to compute activation times for stimuli from all parts of the atria. Potential flutter pathways are then identified by tracing loops from wave front collision sites and constricting them using a geometric snake approach under consideration of the heterogeneous wavelength condition. In this way, all pathways along which AFlut can be sustained are identified. Flutter pathways can be instantiated by using an eikonal-diffusion phase extrapolation approach and a dynamic multifront fast marching simulation. In these dynamic simulations, the initial pattern eventually turns into the one driven by the dominant pathway, which is the only pathway that can be observed clinically. We assessed the sensitivity of the flutter pathway maps with respect to conduction velocity and its anisotropy. Moreover, we demonstrate the application of tailored models considering disease-specific repolarization properties (healthy, AF-remodeled, potassium channel mutations) as well as applicability on a clinical dataset. Finally, we tested how AFlut vulnerability of these substrates is modulated by exemplary antiarrhythmic drugs (amiodarone, dronedarone). Our novel method allows to assess the vulnerability of an individual patient to develop AFlut based on the personal anatomical, electrophysiological, and pharmacological characteristics. In contrast to clinical electrophysiological studies, our computational approach provides the means to identify all possible AFlut pathways and not just the currently dominant one. This allows to consider all relevant AFlut pathways when tailoring clinical ablation therapy in order to reduce the development and recurrence of AFlut.

**Keywords:** atrial flutter, ablation, vulnerability, computational modeling, personalized model

## 1. INTRODUCTION

The long-term success rate of atrial fibrillation (AF) ablation is unsatisfactory low, particularly in patients suffering from persistent AF. Besides AF recurrence, the development of post-ablational atrial flutter (AFlut) represents a major problem (Villacastín et al., 2003; Kobza et al., 2004; Chugh et al., 2005; Patel et al., 2008; Yamada and Kay, 2013; Biviano et al., 2015). In more than half of the patients, sustained AF is reinitiated within 5 years after ablation or AFlut develops (Bunch et al., 2016). 20% of recurrences after AF ablation in elderly are due to AFlut (Dong et al., 2015). In the general AF population, 18.5% of patients were diagnosed with AFlut during a median follow-up time of 421 day post ablation (Gucuk Ipek et al., 2016). Liang et al. (2015) observed AF or organized atrial tachycardia in 53% of 300 patients within the first 6 weeks after pulmonary vein (PV) isolation. AF and AFlut are often even combined endpoints in studies evaluating the success of AF ablation (Bunch et al., 2016). Waldo and Feld (2008) highlighted the inter-relationship between AF and AFlut. AF precedes AFlut in most cases forming the required line of block by fibrillatory conduction. Moreover, ablation of atrial tissue can lead to a substrate for AFlut. Particularly gaps in linear lesions forming isthmuses or revitalized tissue areas forming zones of slow conduction render the atria vulnerable. Also PV isolation has been associated with a substantial risk to develop AFlut (Mesas et al., 2004; Deisenhofer et al., 2006; Jaïs et al., 2006). Castrejón-Castrejón et al. (2011) reviewed the occurrence of organized atrial tachycardia such as AFlut after AF ablation and emphasize that more extensive left atrium (LA) ablation renders the patient more vulnerable to AFlut. However, the exact origin of the pathologic substrate is not understood. Therefore, we present a method to assess the vulnerability to AFlut in personalized computational models. Besides an identification of possibly AFlut sustaining pathways in the observed state of the patient (*baseline*), the approach allows to assess the effect of different therapeutic strategies such as ablation patterns, pharmacological compounds, or other anatomical and electrophysiological interventions *in silico* before actually performing them *in vivo*.

A common approach to simulate complex excitation patterns is the monodomain reaction-diffusion model which is based on the transport of ions within the domains and across the cell membrane (Niederer et al., 2011). As such, it considers electrotonic effects and source-sink relations resulting in e.g., convex or concave wavefronts. On the one hand, the monodomain approach provides the means to study complex and chaotic patterns such as fibrillation including wave breaks. On the other hand, the monodomain model is computationally expensive even using optimized implementations (Labarthe et al., 2014; Pezzuto et al., 2017). Hence, a thorough exploration of the parameter space regarding effects on the three-dimensional whole organ level, as e.g., the vulnerability to arrhythmia caused by ectopic stimuli from a multitude of locations and at varying time instants, is infeasible. Eikonal approximations of the continuous dynamics of the reaction-diffusion system allow to simulate excitation propagation in terms of activation times with significantly reduced computational load by several

orders of magnitude (Wallman et al., 2012; Labarthe et al., 2014; Loewe, 2016; Neic et al., 2017; Pezzuto et al., 2017) as only one static, non-linear partial differential equation derived from the monodomain model has to be solved, which makes it interesting for simulations of cardiac activation (Keener, 1991; Franzone and Guerri, 1993). In contrast to level set methods in general, shortest pathway (van Dam and van Oosterom, 2003) and fast marching methods assume monotonously expanding wavefronts. Thus, a specific approach considering multiple fronts, reentry, and anisotropic conduction was developed for cardiac electrophysiology (Sermesant et al., 2007; Pernod et al., 2011) based on the fast marching method on structured grids (Sethian, 1996, 1999; Sermesant et al., 2005). Several extensions provide the means to consider wavefront curvature and the mesh structure if that is needed for the specific application (Sethian and Vladimirovsky, 2000, 2003). Ablation of ventricular tissue in order to prevent scar-related ventricular tachycardia was presented as a potential application for this method (Pernod et al., 2011). However, one should keep in mind that while current multifront fast marching methods faithfully represent macro-reentrant arrhythmias like AFlut, they are not well suited to study more complex reentries like spiral wave or multiple wavelet reentry where local source-sink mismatch plays a crucial role (Loewe, 2016).

The aim of this work is to develop a method that allows to comprehensively assess the vulnerability to AFlut in personalized models considering both anatomical and electrophysiological properties allowing to evaluate therapeutic approaches such as ablation and drug treatment *in silico*.

## 2. MATERIALS AND METHODS

A simulation pipeline consisting of several steps (**Figure 1**) was developed in order to assess the vulnerability to AFlut. In this section, the different building blocks of the workflow are presented.

### 2.1. Fast Marching Simulation of Excitation Propagation

The eikonal equation governs the spread of an activation wave in a possibly anisotropic medium resulting in a scalar field  $t_a(x_i)$  – the activation map:

$$c\sqrt{\nabla t_a \vec{G} \nabla t_a} = 1, \quad (1)$$

with  $c(x_i)$  being the speed function defined for each node  $x_i$ ,  $t_a(x_i)$  being the activation time, and  $\vec{G}$  being a tensor enabling anisotropy to account for faster conduction along the principal axis of myocytes than perpendicular to it (Loewe, 2016):

$$\vec{G} = R(\phi, \theta) \begin{pmatrix} k & 0 & 0 \\ 0 & 1 & 0 \\ 0 & 0 & 1 \end{pmatrix} R(\phi, \theta)^T, \quad (2)$$

with  $R(\phi, \theta)$  rotating the coordinate system to align the positive x-axis with the principal myocyte orientation. The multifront fast marching scheme for the eikonal-based simulation of

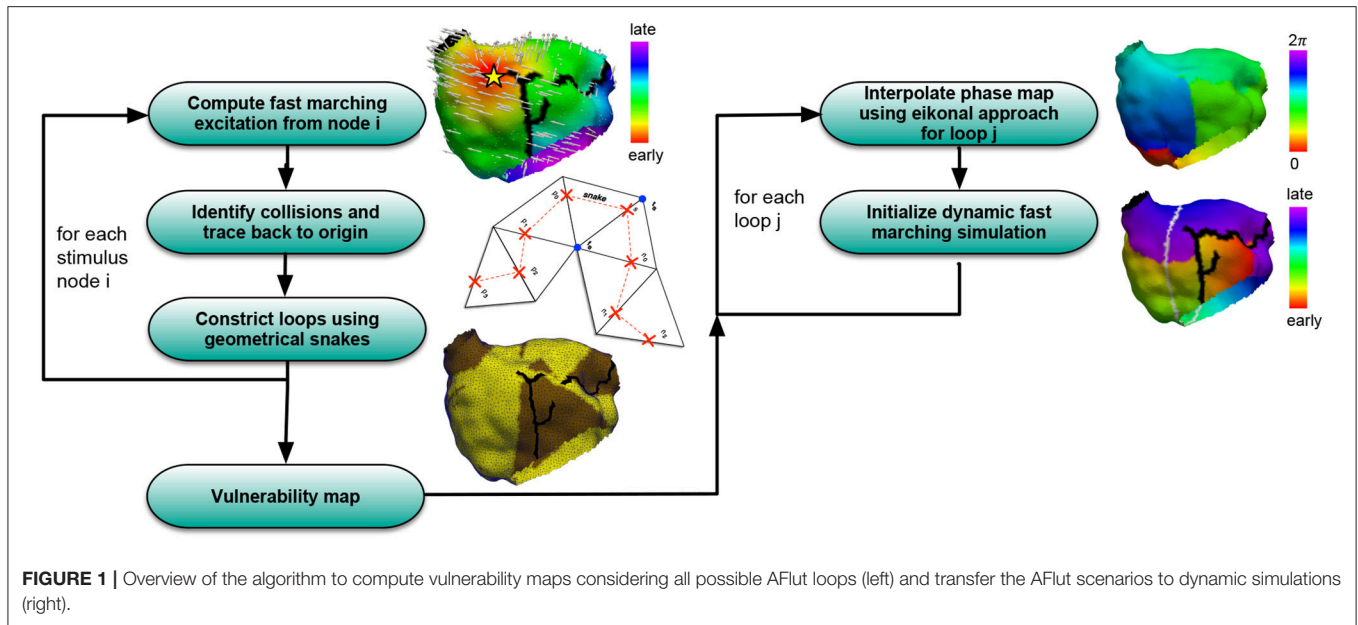


**FIGURE 1** | Overview of the algorithm to compute vulnerability maps considering all possible AFut loops (left) and transfer the AFut scenarios to dynamic simulations (right).

excitation propagation introduced by Sermesant et al. (2007) (**Supplementary Algorithm 1**) was extended to consider restitution of conduction velocity (CV) and effective refractory period (ERP). Restitution of both parameters with respect to basic cycle length (BCL) was determined by pacing in a one-dimensional tissue strand using the Courtemanche et al. cell model (Courtemanche et al., 1998) coupled in a monodomain approach as detailed in Wilhelms et al. (2013). These restitution curves provide opportunities for functional model personalization in the future as further discussed below. The resulting curves for CV were approximated by fitting to exponential decays:

$$CV(BCL) = A - B \cdot \exp\left(-\frac{BCL}{C}\right). \quad (3)$$

The BCL was defined as the time passed since the last activation of the respective node and initialized with a user-defined value either globally or for each node individually. The restitution of the ERP was described the same way.

## 2.2. Identification of Flutter Loop Candidates

The fast marching approach was used to trigger excitations from a multitude of locations sequentially. For each stimulus location, activation times were computed and stored together with information regarding the spread of excitation in terms of a vector pointing from the activating to the activated node. Wavefront collision sites were defined as points of latest activation on circular pathways composed of two traces originating from the stimulus site to opposite sides, i.e., at an angle of approximately  $\pi$ . On the one hand, these pathways are the shortest in the sense of wave propagation, i.e., they are not artificially prolonged by zig-zag patterns but determined as the shortest connection by the fast marching algorithm. On

the other hand, they are locally the longest as two independent waves collided on the loop. A wavefront collision for node  $i$  was identified if the following condition was fulfilled for any neighboring node  $j$ :

$$\frac{\vec{a}_i}{\|\vec{a}_i\|_2} + \frac{\vec{a}_j}{\|\vec{a}_j\|_2} < 0.99, \quad (4)$$

with  $\vec{a}_i/\vec{a}_j$  being the vector pointing from the node that activated node  $i/j$  to node  $i/j$  itself. The condition identifies all points at which the vectors meet at an angle  $\in (\pi/2, 3\pi/2)$ , thus pointing in opposite directions. From the sites of collisions, loops were defined by the two traces along the steepest negative activation time gradient leading back to the stimulus location. A loop was thus composed of a circular, ordered series of nodes. Along the loop, the round trip time (RTT) was calculated considering the heterogeneous and anisotropic tissue properties in terms of CV. If a loop did not fulfill the wavelength (WL) condition

$$\max_i (ERP_i(RTT)) < RTT, \quad (5)$$

it was disregarded. Here,  $ERP_i$  is the ERP of node  $i$  considering a BCL equal to the RTT according to Equation (3).  $i$  iterates over all nodes spanning the loop candidate.

## 2.3. Constriction of Flutter Loop Candidates

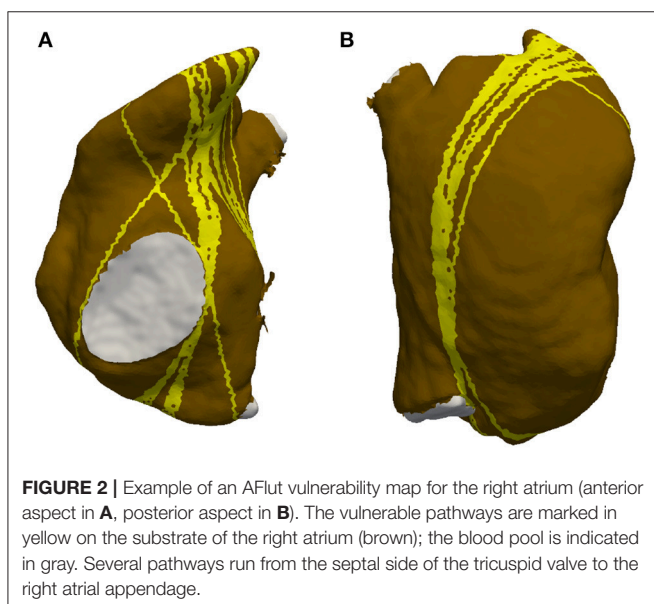
The fact that the loops were traced back all the way to the initial stimulus site introduced artifacts as a dynamic wave would cut short between the two traces from the site of collision to the stimulus site in many cases. In the easier case, both half loops share a part of the loop. Under such circumstances, all common nodes can be neglected, thus shrinking the loop (**Supplementary Figure 1A**). In most

cases, however, artifacts of other types were present as well. In **Supplementary Figure 1B**, a shortcut of the two half loops running adjacent on the posterior LA wall can be anticipated between the posterior interatrial connections and the connection via the coronary sinus. Therefore, a geometric snake approach (**Supplementary Figures 2, 3**) considering anisotropy was implemented in order to constrict the loops like a rubber band by minimizing the spline energy. Evolving snakes on triangular meshes were proposed before for mesh scissoring operations and constriction detection (Lee and Lee, 2002; Hétoy and Attali, 2003; Bischoff and Kobbelt, 2004; Lee et al., 2004) and were adapted to the requirements of the specific application in this work as further detailed in the **Supplementary Methods**.

## 2.4. Eikonal-Diffusion Phase Extrapolation

The methods introduced above allow to identify pathways in an atrial model that can potentially sustain AFlut. However, the pathways are not necessarily dominant and might thus not be expressed in dynamic scenarios. An example is shown in **Figure 2** where several pathways run from the septal side of the tricuspid valve to the right atrial appendage and to the coronary sinus region. Each pathway is locally the shortest and long enough to sustain AFlut according to the WL condition. However, according to Huygen's principle, only one pathway will dominate the excitation pattern distal to the constriction at the tricuspid valve where all pathways narrow. Thus, the remaining pathways will be suppressed. In order to identify the dominant pathway, i.e., to distinguish between theoretically vulnerable pathways and practically inducible pathways, the initial state for a dynamic simulation can be extrapolated from a single loop to the entire simulation domain as detailed in the **Supplementary Methods**.

**Figure 1** summarizes the pipeline used to generate AFlut vulnerability maps and transfer the results to dynamic simulations.



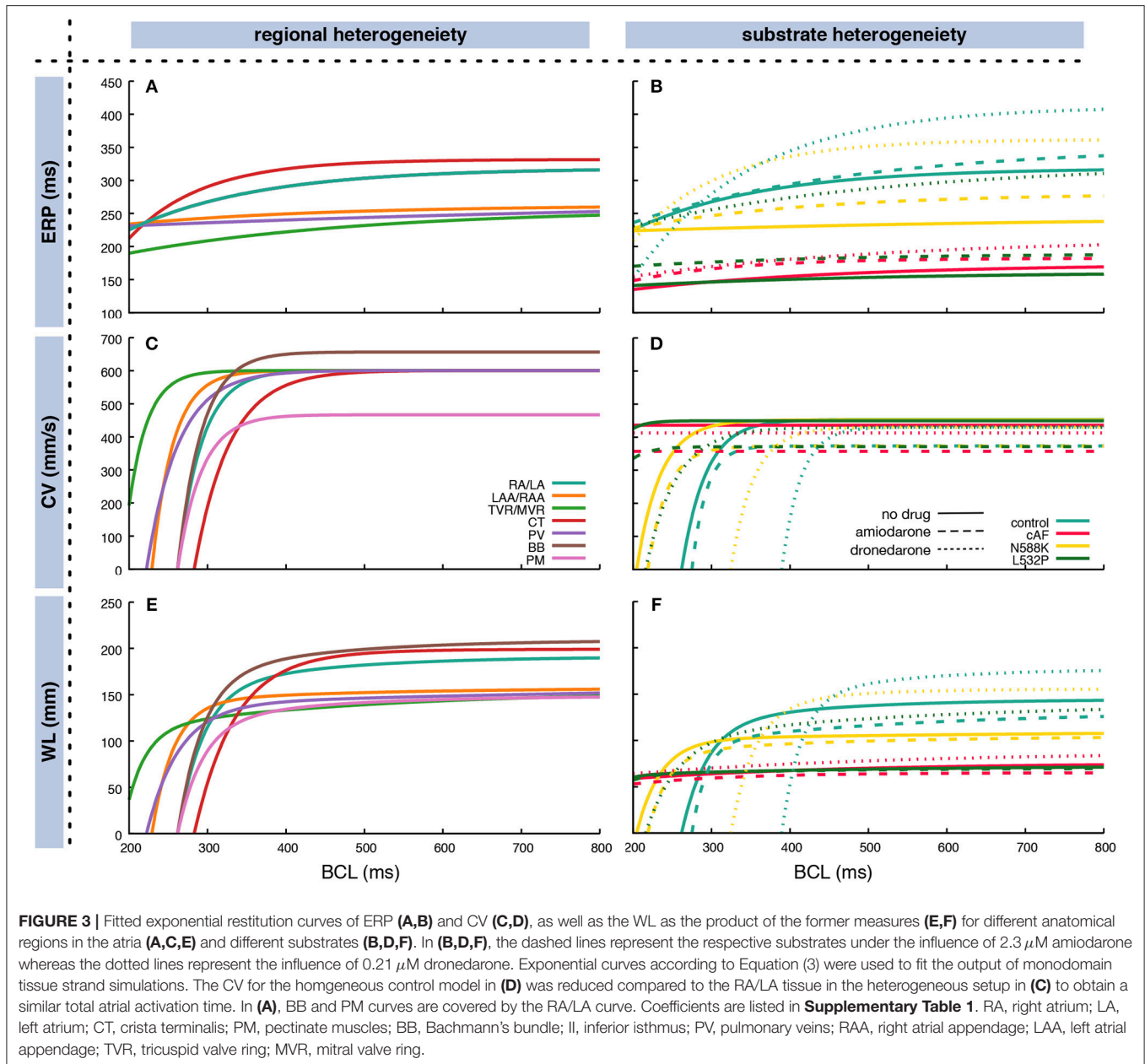
## 2.5. Heterogeneous Tissue Properties, Disease-Specific Substrates, and Drug Effects

The restitution of CV and ERP was determined through monodomain simulations in a one-dimensional tissue strand as detailed in Wilhelms et al. (2013). CV and ERP were determined for 50 BCLs between 200 and 1,000 ms distributed linearly in frequency domain. Regional heterogeneity between different anatomical areas within the atria was accounted for as described previously in terms of both electrophysiological properties (Krueger et al., 2013) and monodomain conductivities (Loewe et al., 2015) in a heterogeneous setup. Furthermore, four different atrial substrates were analyzed in homogeneous setups: (i) a control substrate representing healthy myocardium modeled by the original Courtemanche et al. (1998) cellular model, (ii) a substrate which has undergone remodeling due to chronic atrial fibrillation (cAF) (Loewe et al., 2014b), (iii) a substrate with the N588K mutation in the human ether-à-go-go-related gene (hERG) (Loewe et al., 2014c), and (iv) a substrate with hERG mutation L532P (Loewe et al., 2014c). The latter two substrates have been associated with familial AF and are used here to demonstrate how patient-specific information like genotype-specific repolarization properties can be included in the overall workflow. All four substrates were investigated with and without the influence of two exemplary antiarrhythmic drugs to demonstrate how not only ablation but also drug therapy can be considered and evaluated using our method. Based on a previous study (Loewe et al., 2014a), the class III antiarrhythmic compounds amiodarone and dronedarone were chosen and modeled as detailed there. **Figure 3** shows the exponential fit of the restitution curves based on the coefficients in **Supplementary Table 1**. The CV for the homogeneous control model was reduced compared to the RA/LA tissue in the heterogeneous setup to obtain a similar total activation time.

The ERP for long BCLs ranged between 256 ms for the tricuspid and mitral valve rings to 332 ms for the crista terminalis. Crista terminalis, Bachmann's bundle, and the working myocardium showed a steeper decrease toward shorter BCLs compared to the remaining regions (**Figure 3C**). Regarding AFlut vulnerability, the WL is the decisive factor. Both, different regions and different substrates, exhibited distinct behavior at different BCLs. For example, at short BCLs, crista terminalis was the region with the shortest WL opposed to long BCLs where it was the region with the longest WL together with Bachmann's bundle (**Figure 3E**).

## 2.6. Clinical Example

The proposed method was applied to a clinical example from a 70 year-old female patient who underwent electroanatomical mapping due to atypical AFlut after previous ablation for AF. The previous AF ablation comprised PV isolation, ablation of a mitral isthmus line and the cavotricuspid isthmus. The patient presented with atypical AFlut with a cycle length of 420 ms. Mapping was performed using the Rhythmia system (Boston Scientific, Marlborough, MA, USA). The PVs were still isolated, electrogram voltage along the mitral isthmus line was reduced



but the line was not blocked. A zone of slow conduction was identified on the left anterior wall close to the left PVs. Five different AFlut types with cycle lengths between 280 and 470 ms could be induced clinically. The arrhythmia terminated to sinus rhythm upon the first ablation in the zone of slow conduction. Further ablation points were placed in the area of the anterior line and connected to the mitral valve. Afterwards, tachycardia could not be induced anymore by burst pacing from the coronary sinus with cycle lengths down to 200 ms. The LA geometry acquired during the procedure comprising 7,471 nodes was retrospectively exported from the clinical system and transferred to the fast marching simulation environment. The previous ablations were manually annotated in the patient LA geometry (Figure 10A).

To reproduce the clinical reentry pattern and activation map qualitatively, the CV was homogeneously set to 650 mm/s and the ERP to 250 ms. The protocol was approved by the ethics committee of the University of Freiburg. The subject gave written informed consent in accordance with the Declaration of Helsinki.

### 3. RESULTS

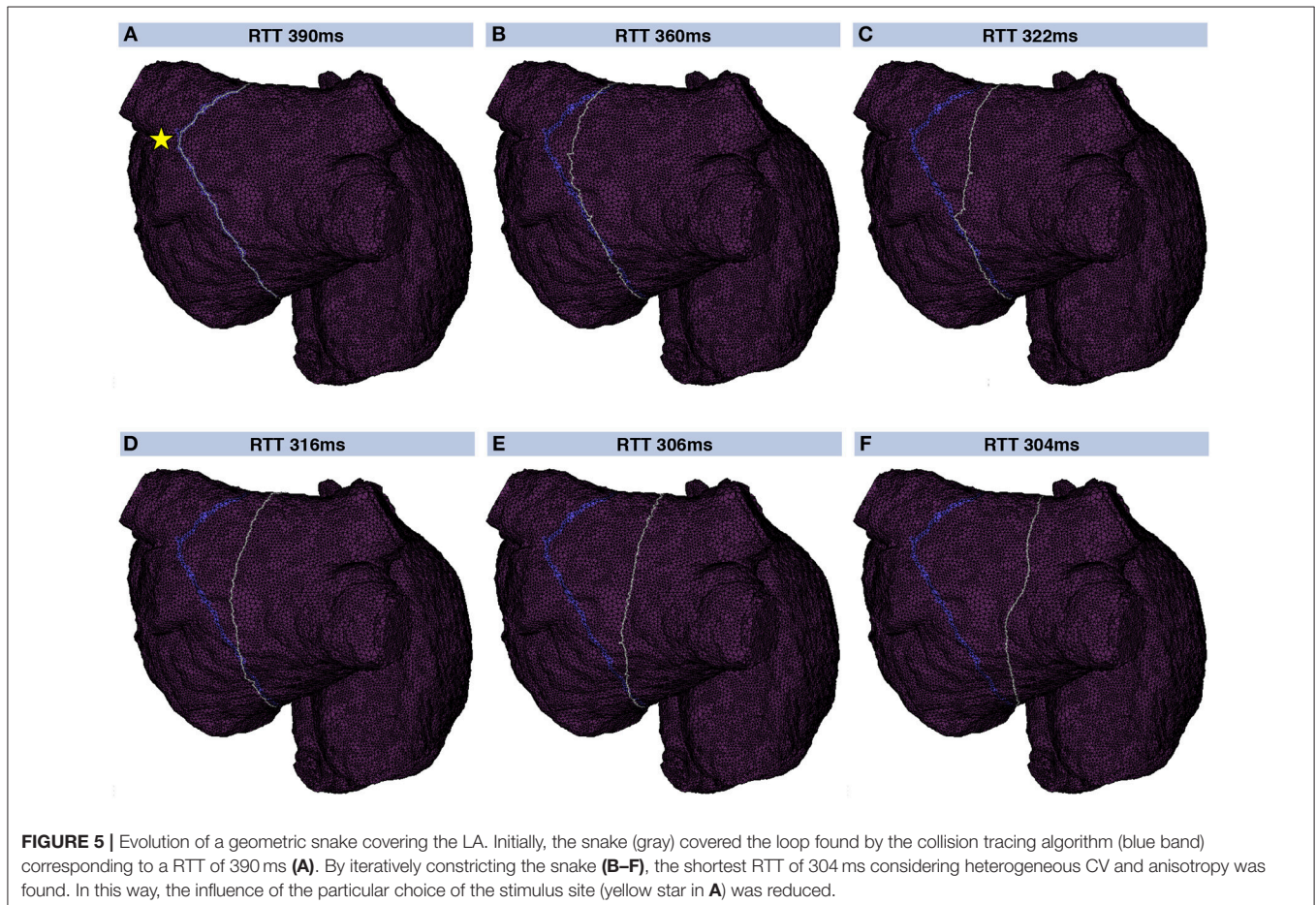
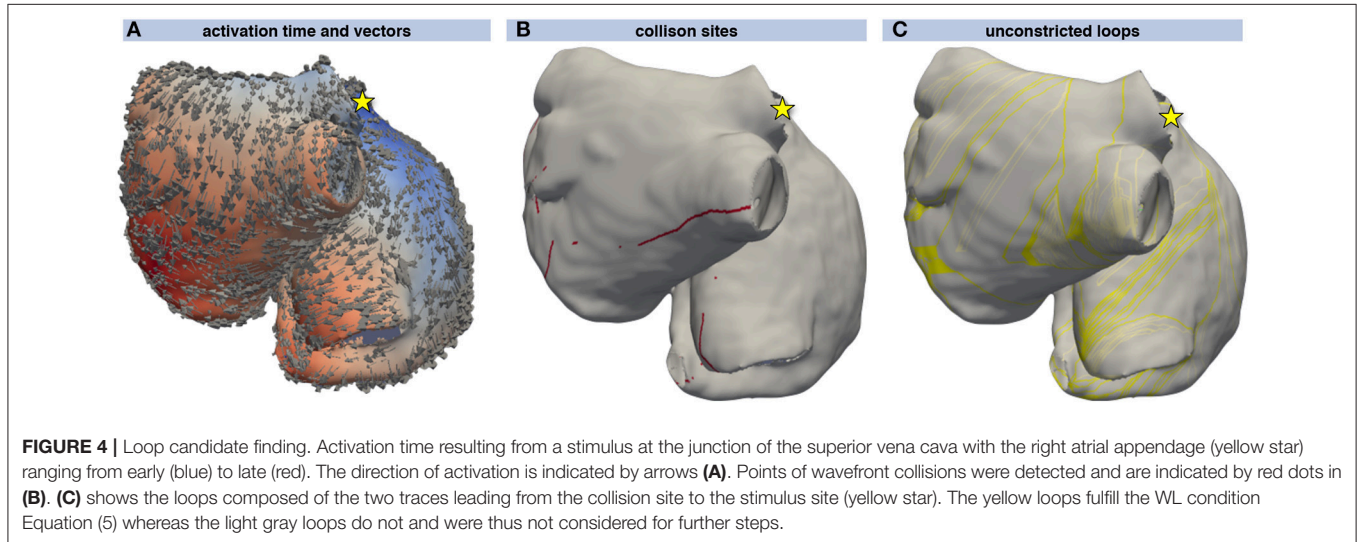
#### 3.1. Flutter Loops and Geometric Snakes

Excitation propagation was calculated from several stimulus locations and sites of collision were detected using the activation vectors as shown in Figures 4A,B. From the sites of wavefront collision, the activation front was traced back

to the stimulus site along the gradient of the activation time field. Combining the traces obtained by following the activation waves of both colliding waves yielded a set of initial loops for each stimulus node (**Figure 4C**). The WL condition Equation (5) was not fulfilled by several loops that could thus be

neglected during the following steps (lighter colored loops in **Figure 4C**).

A geometrical snake was initialized for each valid loop candidate. **Figure 5** shows a geometrical snake initialized along a flutter loop candidate in the LA. The stimulus leading to



that loop was applied between the two left PVs (yellow star in **Figure 5A**). The segment connecting the loop candidate with the stimulus location was shared by both half loops and disregarded before the snake was initialized. The initial RTT of 390 ms was reduced to 304 ms by iterating the snake according to **Supplementary Equation (4)**. The converged snake reflects myocyte orientation and CV heterogeneity (**Figure 5F**).

### 3.2. Vulnerability Maps

By triggering stimulation from different points, identifying loop candidates, and constricting them using geometrical snakes, AFLut vulnerability maps were generated as outlined in **Figure 1**. In a first step, an MRI-derived triangular mesh of the RA comprising 19,296 nodes augmented with rule-based tissue labels and myocyte orientation (Wachter et al., 2015) was used. The triangular surface model is a lumped representation of the atrial wall with a single myocyte orientation in each element. As detailed in Wachter et al. (2015) and Loewe (2016), crista terminals and the pectinate muscles were integrated within the RA wall. The vulnerability maps were sensitive to tissue anisotropy as indicated by the lower number of flutter pathways in the isotropic models (**Figures 6A,C**) compared to the anisotropic cases (**Figures 6B,D**). While the heterogeneous *A* and *B* values defining the CV according to Equation (3) were scaled in the isotropic and homogeneous cases to match the sinus rhythm activation time of the last element in the heterogeneous anisotropic simulation, both anisotropy and heterogeneity increased the number of vulnerable pathways. In the homogeneous isotropic setup (**Figure 6A**), only 12.7% of all elements were covered by vulnerable pathways. Adding

anisotropy (**Figure 6B**) increased the coverage to 20.8% whereas adding heterogeneity (**Figure 6C**) lead to 15.9% coverage. 51.7% of the fully heterogeneous and anisotropic model (**Figure 6D**) were covered by vulnerable pathways.

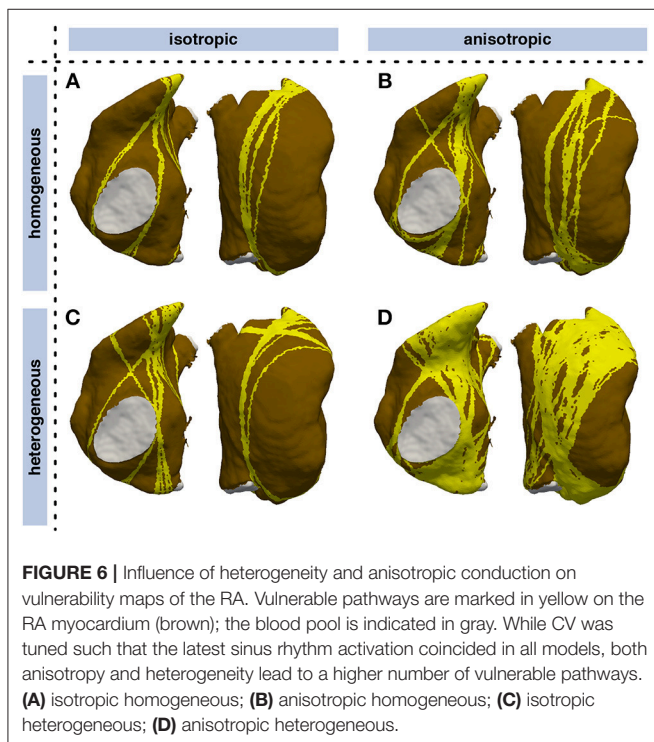
The number of vulnerable pathways and the share of RA myocardium covered by them was highly dependent on the CV. In a homogeneous anisotropic setup (ERP 318 ms at long BCLs), the coverage increased from 0% at a CV of 475 mm/s to over 90% for CVs of 360 mm/s and lower (**Figure 7A**). When interpreting these findings, one should keep in mind the homogeneous ERP restitution used in this experiment (solid green line in **Figure 3B**). The degree of coverage also depends on the number of different stimulus locations evaluated (**Figure 7B**). Considering all 19,296 RA nodes yielded a coverage of 54.5% for a fixed CV of 425 mm/s. Requiring a minimum distance of 1 mm between stimulus points reduced their number to 8,254 without affecting the coverage result markedly (50.9%). Considering less points yielded lower coverage rates (39.4% for 2 mm  $\hat{=}$  2,136 nodes, 3.8% for 20 mm  $\hat{=}$  19 nodes).

The degree of coverage was highly dependent on the substrate as detailed in **Table 1**. 8,254 stimulus points with a minimum distance of 1 mm were considered using the CV and ERP values fitted from the monodomain model output using the biophysically detailed cell models given in **Supplementary Table 1**. While the fitted exponential restitution of ERP and CV was modeled homogeneously across the RA, its region-dependent heterogeneous anisotropy (*k* in **Supplementary Table 1**) was kept. To operate in an interesting range of vulnerability (**Figure 7A**), CV at long BCLs (*A* in **Supplementary Table 1**) was set to 454 mm/s in the following yielding a total RA activation time of 194 ms in the *control* model without any drug applied.

Both the cAF substrate and the two hERG mutations were more vulnerable to AFLut than the control model representing healthy myocytes. The higher degree of coverage under the influence of amiodarone observed for all substrates can be explained by the WL restitution (**Figure 3F**). The WL was shortened by the administration of amiodarone due to conduction slowing caused by the sodium channel inhibition. This effect was most pronounced in the control substrate and was reflected in the vulnerability maps as well (**Figure 8**).

In order to separate the effects of the different substrates and compounds on CV and ERP, the total activation time of the RA was matched with the activation of the last element in the control model and no drug (192 ms) in a second set of simulations (**Supplementary Figure 4**), i.e., the *A* and *B* parameters determining the CV according to Equation (3) were scaled while keeping the anisotropy ratio *k* constant. In this way, only the effect on repolarization (ERP) was considered leading to a reduction of vulnerable pathways under the influence of amiodarone in all substrates and a more pronounced reduction under the influence of dronedarone compared to **Figure 8**.

Besides evaluating different substrates, distinct spatial heterogeneities were introduced in the RA model. The normal RA myocardium was parametrized with an isotropic CV of 700 mm/s and an ERP of 250 ms for all BCLs. A circular zone of slow conduction on the posterior wall was modeled



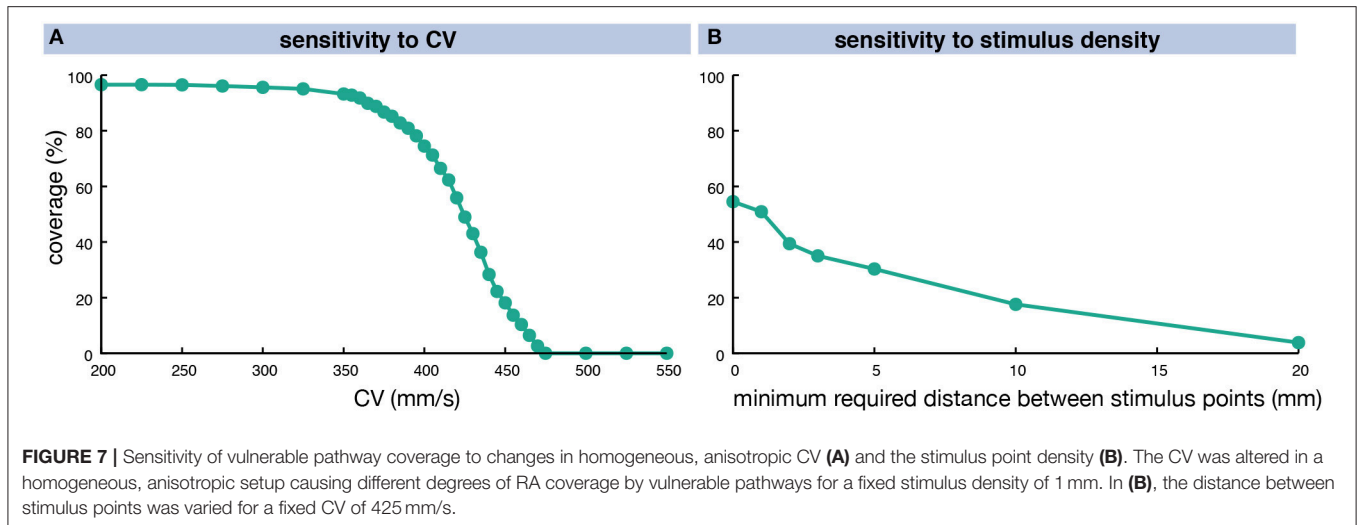


**TABLE 1 |** Degree of coverage of RA elements with pathways vulnerable to AFlut for different substrates and antiarrhythmic drugs amiodarone (*amio*) and dronedarone (*drone*).

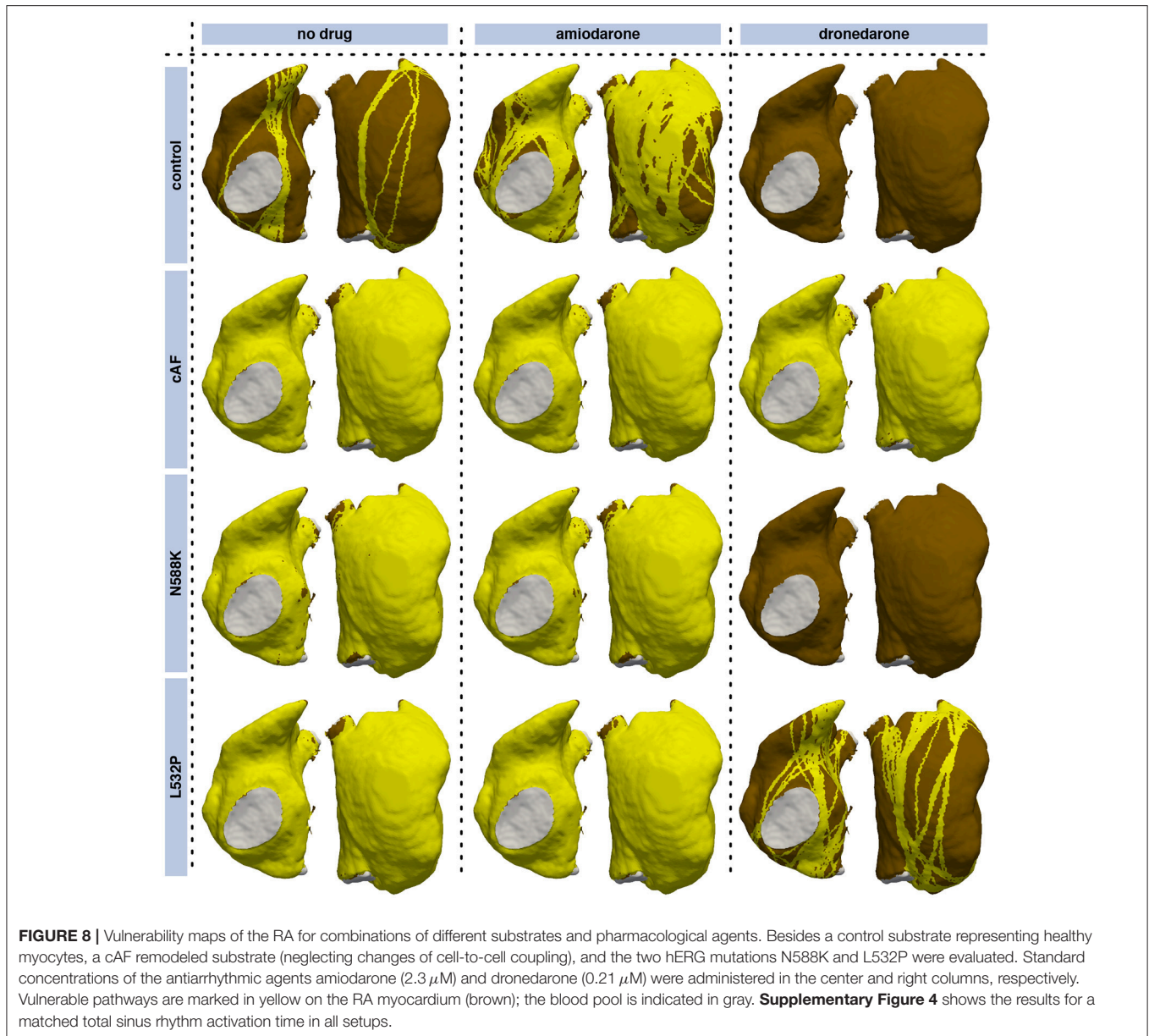
|         | Degree of coverage |       |       |                               |       |       |
|---------|--------------------|-------|-------|-------------------------------|-------|-------|
|         | Original CV        |       |       | Total activation time matched |       |       |
|         | no drug            | amio  | drone | no drug                       | amio  | drone |
| Control | 18.1%              | 70.5% | 0.0%  | 18.1%                         | 0.0%  | 0.0%  |
| cAF     | 96.0%              | 96.3% | 95.6% | 96.2%                         | 96.1% | 94.9% |
| N588K   | 93.2%              | 94.1% | 0.0%  | 93.0%                         | 77.8% | 0.0%  |
| L532P   | 96.2%              | 96.5% | 34.5% | 96.3%                         | 96.0% | 11.1% |

In the right three columns, the A and B values determining the CV according to Equation (3) were scaled to match the activation time of the last element during sinus rhythm in the control substrate with no drug applied.

(Figures 9B,C). Depending on the CVs inside and outside this zone, the wave might be faster bypassing the zone than propagating through it. Comparing the time the wave takes to bypass the circle with the time it takes to propagate through the zone of slow conduction yields a critical  $CV_{slow}/CV_{normal}$  ratio of  $2/\pi \approx 0.63$ . If the ratio is higher, the dominant pathway is through the zone of slow conduction. If it is lower, the bypassing wave is faster. Therefore, the zone of slow conduction within the surrounding tissue conducting at 700 mm/s was parametrized with a CV of 500 mm/s resulting in a ratio of 0.71 (Figure 9B), and 250 mm/s ( $\approx 0.36$ , Figure 9C). In contrast to the control model (Figure 9A), the zones of slow conduction yielded additional flutter pathways. For the CV of 500 mm/s in the zone of slow conduction, 24.1% of the RA were covered by vulnerable pathways (Figure 9B) in contrast to 14.1% in the control case (Figure 9A). Additional flutter pathways crossed the periphery of the zone of slow conduction and thereby prolonged the RTT. For the slower CV of 250 mm/s, the entire zone of slow conduction was covered by vulnerable pathways yielding a total RA coverage of 47.8% (Figure 9C). The pathways were not constricted to the faster route outside the zone as the route through the zone of slow conduction was optimal considering the field of view of the geometrical snake. When computing an inducibility map (see Discussion), the driving pathway would be running around the zone of slow conduction, though.

The second spatial substrate modification was an ablation lesion which encircled the RA completely (Figure 9D). Rather than being a clinically used ablation pattern, this scenario serves as an example separating the RA into two electrically isolated regions. The lesion was modeled as non-conductive, thus no flutter pathways could cross it. In additional scenarios, a gap in the ablation lesion of varying extent was assumed at the central posterior wall (Figures 9E,F). In case of the complete lesion, no flutter pathways were identified (Figure 9D) as the WL condition could not be fulfilled on any of the two separated, smaller substrates. The gap in the ablation lesion yielded numerous vulnerable pathways running through the gap at various angles (Figure 9E). The flutter pathways covered 42.9% of the RA in contrast to 14.1% in the control case, thus the ablation increased AFlut vulnerability markedly. In case of a smaller gap (Figure 9F), the number of loops was smaller than for the wider gap as the narrow gap served as a funnel. Nevertheless, the coverage (23.3%) was still markedly higher than for the control case.

The time to compute a complete vulnerability map depends on the mesh resolution as well as the number of stimulus points considered and the number of loop candidates fulfilling the WL condition over time. The computation is faster, the fewer loop candidates there are and the earlier the constricted loops are disregarded because they no longer fulfill the WL



condition (data not shown). For the RA mesh consisting of 19,296 nodes, computation was timed on an *Intel Xeon E5-2697V2* machine with twelve cores at a base clock rate of 2.7 GHz. The control vulnerability map in **Figure 9A** with a coverage of 14.1% was computed within 4.0 min whereas it took 5.5 min to compute the vulnerability map for the RA including the zone of slow conduction yielding a coverage of 47.8% (**Figure 9C**).

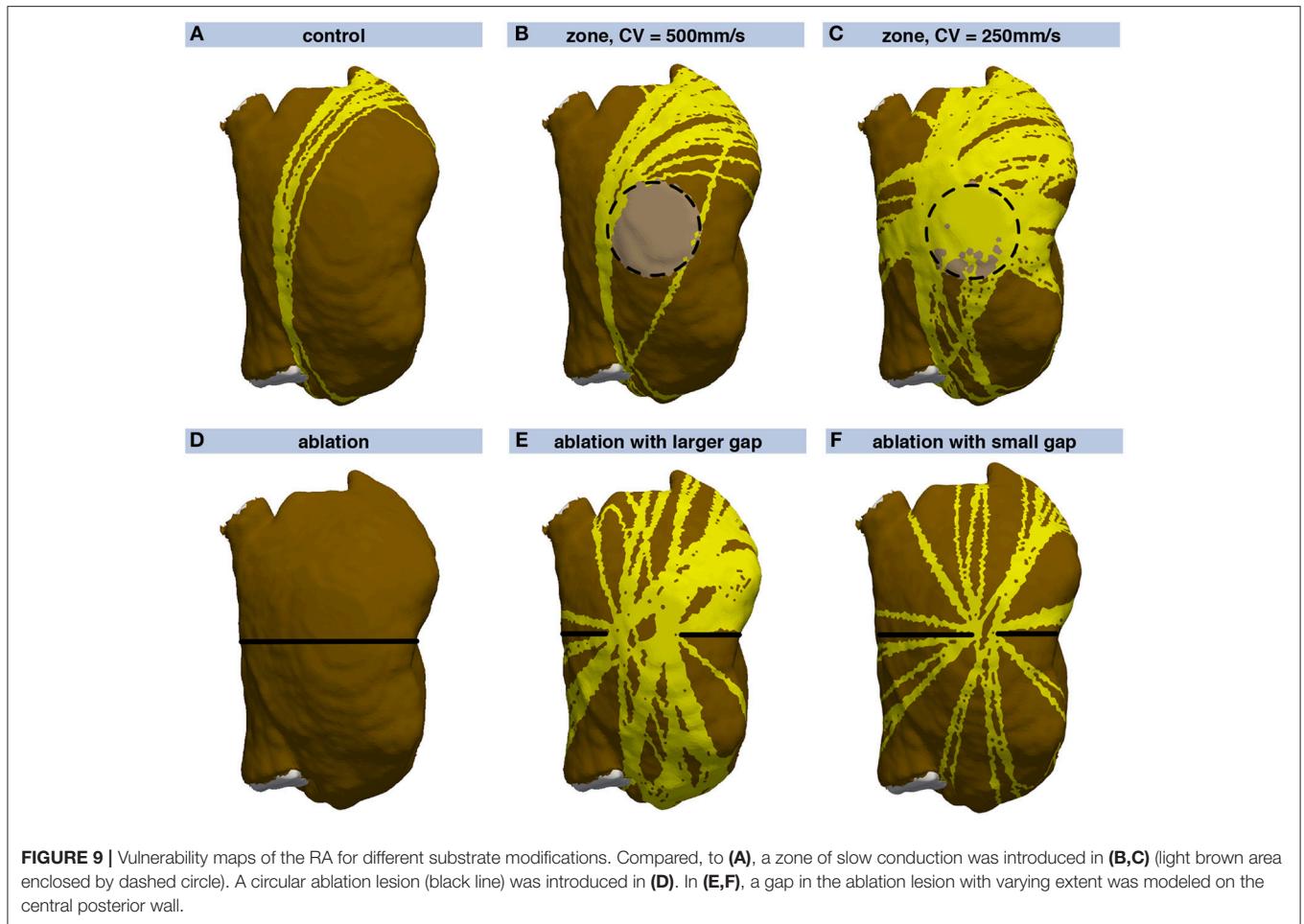
### 3.3. Phase Extrapolation

The vulnerable pathways represented in the vulnerability maps and identified using the methods described above were extrapolated on the whole RA in terms of phase using the methods described in section 2.4. Each vulnerable pathway was extrapolated in phase space individually. The eikonal-diffusion

approach converged within 16 to 18 iterations and was robust against variations of the CV [**Supplementary Equation (7)**] and the RTT [**Supplementary Equation (9)**], i.e., the cycle length of the reentry. CV was varied between  $0.1\times$  and  $2\times$  the ground truth value used in the fast marching simulation and assumed RTTs between  $0.3\times$  and  $3\times$  the ground truth value. The phase map was then used to determine the initial state of a dynamic fast marching simulation as exemplified in the next section for a clinical dataset.

### 3.4. Clinical Example

The initial vulnerability map representing the state with which the patient presented for the redo procedure (compare section 2.6) covered most parts of the LA (**Figure 10A**). Aflut pathways



running through the gap in the anterior line were present. After closing this gap, the left part of the anterior wall became free from AFlut pathways and they were restricted to the central part of the posterior wall (**Figure 10B**). However, there were still numerous AFlut pathways remaining. These pathways (the gray line in **Figure 10D** shows one example) were used to extrapolate a phase map on the whole domain (**Figure 10C**) and initialize a dynamic fast marching flutter simulation (**Figure 10D**). Reentry was stable for the entire simulation duration of 100 reentrant cycles. After connecting the line on the anterior wall to the RSPV by additional ablation, no more vulnerable pathways could be identified (**Figure 10E**).

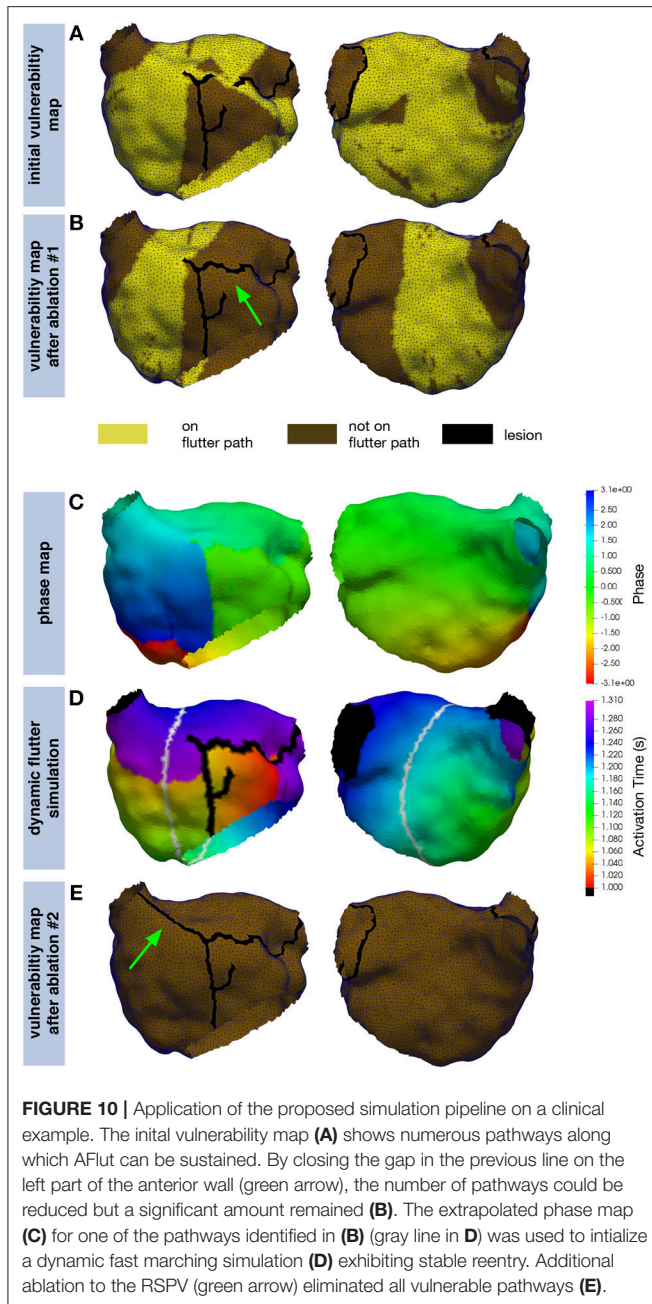
## 4. DISCUSSION

### 4.1. Main Findings

In this study, a simulation workflow to identify vulnerable pathways potentially sustaining AFlut was presented. The approach builds on personalized fast marching simulations of excitation propagation and geometric snakes to constrict pathways identified on the basis of wavefront collision sites. Throughout the whole pipeline, heterogeneous, anisotropic, and

heart rate-dependent tissue properties are considered in terms of CV and ERP.

The geometrical snake approach presented by Bischoff and Kobbelt (2004) was adapted to the excitation propagation application scenario considering the tissue property heterogeneities mentioned above. Applying the geometric snake approach to loop candidates identified as circular pathways from an initial stimulus point via a site of wavefront collision back to the initial stimulus yielded AFlut vulnerability maps. The number and the location of the identified vulnerable flutter pathways were sensitive to (i) anisotropy (**Figure 6**), (ii) the substrate properties regarding CV and repolarization, as well as modification of these parameters due to pharmacological compounds (**Figure 8** and **Supplementary Figure 4**), (iii) zones of slow conduction or ablation lesions (**Figure 9**), and most importantly (iv) the assumed CV (**Figure 7**). Anisotropic substrates were more vulnerable than isotropic tissue when matching the total sinus rhythm activation time of the RA. The WL is a crucial parameter as can be seen by the higher number of vulnerable pathways identified for the cAF and hERG mutated substrates compared to control. While dronedarone reduced the AFlut vulnerability, amiodarone rendered the substrate more vulnerable due to the reduced WL caused by



the slowed CV (Figure 3). When only considering the effect on repolarization, thus altering ERP to represent the influence of the drug, amiodarone exhibited antiarrhythmic properties as well. The effect was less pronounced than for dronedarone, though. Zones of slow conduction increased the number and the density of vulnerable pathways as the cycle length increases both by conducting through the slow zone and by bypassing it. Ablation lesions isolating different regions completely rendered the RA invulnerable to AF. However, even a small gap in the lesion increased the number of vulnerable pathways markedly compared to control. This effect can be explained by the narrow isthmus formed by the gap in the lesion and

highlights the importance of lesion durability. When linear lesions are partly revitalizing, they form ideal pathways for AF. In particular, shortcuts leading to wavefront collision and ceasing the reentrant activation are cut off by the lesion, thus stabilizing the reentry. The assumed CV had the biggest effect on the number of vulnerable pathways and the degree of RA coverage by them. A CV slowing by 25% rendered an invulnerable RA model highly vulnerable with a flutter pathway coverage of over 90%. This finding highlights the importance of a reliable CV estimation to draw relevant conclusions from personalized models using the method presented here. The CV of the individual patient has to be measured in a spatially resolved, and preferably heart rate-dependent, manner. Weber et al. (2010, 2011) proposed a method to estimate local CV and its restitution based on a cosine fit method. The advent of new electro-anatomical mapping systems and catheters with improved signal quality as well as sophisticated signal processing approaches gives rise to hope for such CV mapping in the near future (Lacru and Saoudi, 2014; Cantwell et al., 2015; Verma et al., 2018).

The application to a clinical example can be considered a proof of concept. We built on the individual anatomy exported from the mapping system and tailored the substrate to the clinically observed activation pattern. The model prediction and the clinical observations show good qualitative agreement. However, it has to be considered that the substrate was modeled homogeneously apart from the lesions and restitution properties were not taken into account. Therefore the lack of exact quantitative match is not surprising.

The computation of a single activation sequence was faster than real-time, a complete vulnerability map took several minutes. Most of the computational cost was due to the constriction of the loop candidates using the geometrical snake approach. While the time spent to calculate excitation propagation accounted for only a minor share, less complex alternatives to the fast marching algorithm exist. Graph-based approaches, such as the A\* algorithm (Hart et al., 1968; Wallman et al., 2012) or the fastest route algorithm (van Dam et al., 2009) are however only faster if the activation time at only a subset of nodes is needed. Cellular automata on the other hand do not consider quadratic approximation of activation times. The computational complexity of the geometrical snake implementation could be reduced by optimizing the number of neighbors considered for the calculation of the snaxel velocity [Supplementary Equation (4)] and the convergence criteria. Indeed, the approach considering  $N = 30$  neighbors with decreasing weight could be approximated by a spatial multi-grid approach starting with distant neighbors in early iterations and focussing on closer nodes at later iterations. When aiming at an interactive modification of the substrate, e.g., by introducing virtual ablation lesions, results from previous evaluations can be reused for regions not affected by the last modification. Moreover, intermediate results could be precomputed, thus trading memory footprint in for reduced computation time. This potential for optimizations together with parallel computing approaches make interactive assessment of ablation therapy in almost real-time appear achievable.

## 4.2. Relation to Previous Work

Dang et al. (2005) and Reumann et al. (2008) compared different standard ablation patterns for AF using idealized computational models and suggest that PV isolation together with linear lesions is the most effective treatment for AF. However, they did not investigate the vulnerability to AFlut post AF ablation systematically. Hwang et al. (2014) proposed a method to test AF ablation patterns *in silico* using a monodomain approach on anatomically, but not electrophysiologically personalized models. Thus, no substrate information regarding fibrosis, zones of slow conduction or the degree of electrophysiological remodeling is considered. Recently, Alessandrini et al. (2018) presented an *in silico* framework to holistically consider the entire cycle from excitation propagation, catheter deformation, electrogram acquisition and processing to virtual ablation. McDowell et al. (2015) published a proof-of-concept how computational modeling can predict ablation sites terminating rotors driving AF in personalized models including fibrosis distribution. Bayer et al. (2016) evaluated the potency of PV isolation, mitral and roof lines, ablation guided by rotor mapping, and lesions streamlining sinus activation regarding the termination of AF *in silico*. The potential of clinically-derived computational models to optimize catheter ablation of AF was recently reviewed by Zhao et al. (2015). They conclude that high-resolution three-dimensional models of functionally and structurally mapped atria of the exact patient are imperative to provide clinically relevant insights on a personalized level.

Lines et al. (2009) presented a method to parametrize a monodomain simulation in a standard bi-atrial model aiming to incorporate electrograms acquired during electroanatomic mapping studies in order to replicate clinically mapped AFlut *in silico*. The extracellular potentials at 32 computational nodes served as a boundary condition for the solution of the monodomain system. While the algorithm synchronized the simulation to the synthetic reference simulation, the algorithm is computationally expensive and only allows to study clinically observed cases *in silico* but cannot provide information on the vulnerability to AFlut.

While those previous studies assessed ablation patterns regarding the prevention or termination of AF, this is the first work to assess the vulnerability to AFlut based on an individualized anatomical model besides a recent work by Zahid et al. (2016) to the best of our knowledge (see also reviews by Jacquemet, 2016; Boyle et al., 2017). Zahid et al. employed the minimum cut algorithm to predict optimal ablation sites for AFlut in the LA with substantially increased computational effort. Child et al. (2015) introduced the reentry vulnerability index (RVI) as a quantitative metric based on the difference between activation and repolarization intervals at pairs of spatial locations. The RVI correlates with exit sites of scar-related reentrant arrhythmia as commonly observed in the ventricles (Hill et al., 2016). However, it aims at predicting functional lines of block rather than providing a comprehensive map of vulnerable pathways based on the individual geometrical properties. The same holds for a study by Wallman et al. (2013) quantifying the arrhythmogeneity of scar and left-to-right heterogeneity in the ventricles.

Trächtler et al. (2015) used the fast marching implementation presented here for a similar *in silico* reproduction of clinical cases. While both methods allow to test ablation strategies regarding the termination of the specific reentry, they do not allow to draw conclusions regarding the vulnerability to AFlut along other pathways. Thus, these approaches do not provide the means to optimize AF ablation aiming at the prevention of post-ablational AFlut.

## 4.3. Outlook

The method presented here could be further developed regarding two aspects. First, the extrapolated phase map obtained by the eikonal-diffusion approach could not only be used to initialize a fast marching simulation but also to replicate the flutter pathway in a monodomain simulation. Matene and Jacquemet (2012) proposed a suitable approach, which they used to initiate AF by extrapolating phase singularities (Jacquemet, 2010; Herlin and Jacquemet, 2011). By initiating the same flutter loop in both the fast marching and the monodomain environment, the fast marching approach could be further validated with respect to macro-reentry. Second, the dominant flutter pathways sustaining reentry in the dynamic simulations could be tracked and compared to the pathways used to extrapolate the initial state. In this way, not only a map of vulnerable flutter pathways but also a map of inducible flutter pathways could be computed.

Moving forward, the complete simulation pipeline should be validated in the clinical setting once tools for a spatially resolved CV and ERP estimation become available. The anatomical model of the individual patient built from MRI data could be augmented with a priori knowledge (Wachter et al., 2015). CV and ERP would be parametrized using intracardiac measurements (Unger et al., 2017; Verma et al., 2018) and complemented with rule-based assumptions. Preferably, the subjects should be recruited from patients undergoing ablation of AFlut that developed after AF ablation. Ideal validation cases would be formed by patients in which a gap in the initial ablation lesion set is identified during the second procedure. The lesions placed during the initial AF ablation procedure as well as the gap in it would be included in the suggested pipeline as further a priori knowledge. The clinically observed flutter pathway should then be found in the vulnerability and inducibility map. Moreover, the ablation terminating the flutter in the clinical setting should also remove the specific vulnerable pathway from the map. In this way, the concepts and methodologies for both vulnerability and inducibility maps could be clinically validated.

## 4.4. Limitations

The implementation of the fast marching algorithm used in this work does consider anisotropic CV but does not consider recursive anisotropic correction as proposed by (Sermesant et al., 2007). In Pernod et al. (2011), the authors of Sermesant et al. (2007) show that the computation time is higher by a factor of  $\approx 1.6$  when considering anisotropic correction. While the influence of the anisotropic correction has never been evaluated systematically, it should not be too relevant for moderate

anisotropy values. For the application presented in this work, subtle differences of the activation sequence do not play a major role for the final result as fast marching activation times serve only as the input for subsequent processing.

Another limitation of the presented method is its restriction to monoatrial flutter pathways. The reason for this can be seen in **Supplementary Figure 5** in which a biatrial loop candidate was constricted using the geometrical snakes approach. While a shortcut within the LA exists, it cannot be resolved by the snake as it is constrained by the interatrial connections and can thus not cross the septum. However, the method could be extended to identify shortcuts within the two atria by also considering monoatrial loops in addition. The final constricted biatrial loop could be used to initialize additional monoatrial loops comprising the segment of the biatrial loop and shortest connection between the two open ends at the interatrial connections. When computing inducibility maps instead of vulnerability maps, this limitation is not relevant since reentry along a loop as in **Supplementary Figure 5** could not be induced if this would not be the case for a comparable monoatrial loop as well. Regarding the dynamic simulation of AFlut, the missing representation of electrotonic coupling is a limitation.

The biggest hurdle is the sparsity of the available clinical data to characterize an individual's substrate and the associated uncertainty. The importance of a reliable CV estimation is highlighted by the fact that a CV uncertainty of  $\Delta c$  corresponds to scaling of the atrium by a factor of  $\sqrt{\Delta c}$  (Jacquemet, 2016). Considering that the minimal WL needed to sustain reentry is defined by the product of CV and ERP, uncertainty of ERP plays an important role as well (Jacquemet et al., 2005; Krogh-Madsen and Christini, 2012; Deng et al., 2017). Improved electro-anatomic mapping systems providing better signal quality and simultaneous mapping using a multitude of electrodes, as well as advanced signal processing methods (Cantwell et al., 2015; Unger et al., 2017; Verma et al., 2018) make it seem probable to have suitable data available in the near future. Moreover, the uncertainty in the data could be taken into account by probabilistic modeling using Bayesian inference and compressed sensing methods (Konukoglu et al., 2011).

## REFERENCES

- Alessandrini, M., Valinoti, M., Unger, L., Oesterlein, T., Doessel, O., Corsi, C., et al. (2018). A computational framework to benchmark basket catheter guided ablation in atrial fibrillation. *Front. Physiol.* 9:1251. doi: 10.3389/fphys.2018.01251
- Bayer, J. D., Roney, C. H., Pashaei, A., Jaïs, P., and Vigmond, E. J. (2016). Novel radiofrequency ablation strategies for terminating atrial fibrillation in the left atrium: a simulation study. *Front. Physiol.* 7:108. doi: 10.3389/fphys.2016.00108
- Bischoff, S., and Kobbelt, L. P. (2004). Parameterization-free active contour models with topology control. *Vis. Comput.* 20, 217–228. doi: 10.1007/s00371-003-0228-9
- Biviano, A. B., Ciaccio, E. J., Fleitman, J., Knotts, R., Lawrence, J., Haynes, N., et al. (2015). Atrial tachycardias after atrial fibrillation ablation manifest different waveform characteristics: implications for characterizing tachycardias. *J. Cardiovasc. Electrophysiol.* 26, 1187–1195. doi: 10.1111/jce.12770
- Boyle, P. M., Zahid, S., and Trayanova, N. A. (2017). Using personalized computer models to custom-tailor ablation procedures for atrial fibrillation

## 4.5. Conclusion

We presented a comprehensive method to analyze the vulnerability to AFlut in a personalized way and demonstrated its applicability for clinical data. The individual anatomy as well as electrophysiology in terms of CV, ERP, and their heart rate dependence is taken into account. This tool provides the means to evaluate potential ablation strategies *in silico* regarding their arrhythmic potential for AFlut before actually applying them in the electrophysiology lab. In this way, this work can be one piece in the puzzle to overcome the *learning by burning* paradigm and eventually reduce the number of patients suffering from post-ablational AFlut.

## DISCLOSURE

Part of this study was published before as a thesis (Loewe, 2016).

## AUTHOR CONTRIBUTIONS

ALo, TO, GS, and OD conceived the study. ALo, EP, and TO implemented the algorithms and performed the *in silico* experiments. ALo, EP, TO, GS, and OD analyzed and interpreted the data. ALu and CS performed the clinical procedure. ALo drafted the manuscript. EP, TO, ALu, CS, GS, and OD revised the manuscript critically. All authors approved the final version of the manuscript.

## FUNDING

This work was supported by Deutsche Forschungsgemeinschaft under grant DFG DO637/22-3, SE1758/3-3, and through CRC 1173. We acknowledge support by Open Access Publishing Fund of Karlsruhe Institute of Technology.

## SUPPLEMENTARY MATERIAL

The Supplementary Material for this article can be found online at: <https://www.frontiersin.org/articles/10.3389/fphys.2018.01910/full#supplementary-material>

- patients: are we there yet? *Expert Rev. Cardiovasc. Ther.* 15, 339–341. doi: 10.1080/14779072.2017.1317593
- Bunch, T. J., May, H. T., Bair, T. L., Jacobs, V., Crandall, B. G., Cutler, M., et al. (2016). The impact of age on 5-year outcomes after atrial fibrillation catheter ablation. *J. Cardiovasc. Electrophysiol.* 27, 141–146. doi: 10.1111/jce.12849
- Cantwell, C. D., Roney, C. H., Ng, F. S., Siggers, J. H., Sherwin, S. J., and Peters, N. S. (2015). Techniques for automated local activation time annotation and conduction velocity estimation in cardiac mapping. *Comput. Biol. Med.* 65, 229–242. doi: 10.1016/j.combiomed.2015.04.027
- Castrejón-Castrejón, S., Ortega, M., Perez-Silva, A., Doiño, D., Estrada, A., Filgueiras, D., et al. (2011). Organized atrial tachycardias after atrial fibrillation ablation. *Cardiol. Res. Pract.* 2011:957538. doi: 10.4061/2011/957538
- Child, N., Bishop, M. J., Hanson, B., Coronel, R., Ophthof, T., Boukens, B. J., et al. (2015). An activation-repolarization time metric to predict localized regions of high susceptibility to reentry. *Heart Rhythm* 12, 1644–1653. doi: 10.1016/j.hrthm.2015.04.013
- Chugh, A., Oral, H., Lemola, K., Hall, B., Cheung, P., Good, E., et al. (2005). Prevalence, mechanisms, and clinical significance of macroreentrant atrial

- tachycardia during and following left atrial ablation for atrial fibrillation. *Heart Rhythm* 2, 464–471. doi: 10.1016/j.hrthm.2005.01.027
- Courtemanche, M., Ramirez, R. J., and Nattel, S. (1998). Ionic mechanisms underlying human atrial action potential properties: Insights from a mathematical model. *Am. J. Physiol. Heart Circ. Physiol.* 275(1 Pt 2), H301–H321.
- Dang, L., Virag, N., Ihara, Z., Jacquemet, V., Vesin, J. M., Schlaepfer, J., et al. (2005). Evaluation of ablation patterns using a biophysical model of atrial fibrillation. *Ann. Biomed. Eng.* 33, 465–474. doi: 10.1007/s10439-005-2502-7
- Deisenhofer, I., Estner, H., Zrenner, B., Schreieck, J., Weyerbrock, S., Hessling, G., et al. (2006). Left atrial tachycardia after circumferential pulmonary vein ablation for atrial fibrillation: incidence, electrophysiological characteristics, and results of radiofrequency ablation. *Europace* 8, 573–582. doi: 10.1093/europace/eul077
- Deng, D., Murphy, M. J., Hakim, J. B., Franceschi, W. H., Zahid, S., Pashkhanloo, F., et al. (2017). Sensitivity of reentrant driver localization to electrophysiological parameter variability in image-based computational models of persistent atrial fibrillation sustained by a fibrotic substrate. *Chaos* 27:093932. doi: 10.1063/1.5003340
- Dong, L., Bie, Z., Sun, L., Pan, X., and Guo, L. (2015). Long-term clinical outcome and risk of catheter ablation in elderly with non-paroxysmal atrial fibrillation. *Int. J. Clin. Exp. Med.* 8, 16050–16056.
- Franzone, P. C., and Guerri, L. (1993). Spreading of excitation in 3-d models of the anisotropic cardiac tissue. I. Validation of the eikonal model. *Math Biosci.* 113, 145–209.
- Gucuk Ipek, E., Marine, J. E., Habibi, M., Chrispin, J., Lima, J., Rickard, J., et al. (2016). Association of left atrial function with incident atypical atrial flutter after atrial fibrillation ablation. *Heart Rhythm* 13, 391–398. doi: 10.1016/j.hrthm.2015.09.028
- Hart, P. E., Nilsson, N. J., and Raphael, B. (1968). A formal basis for the heuristic determination of minimum cost paths. *IEEE Trans. Syst. Sci. Cybern.* 4, 100–107. doi: 10.1109/TSSC.1968.300136
- Herlin, A., and Jacquemet, V. (2011). Eikonal-based initiation of fibrillatory activity in thin-walled cardiac propagation models. *Chaos* 21:043136. doi: 10.1063/1.3670060
- Hétroy, F., and Attali, D. (2003). “From a closed piecewise geodesic to a constriction on a closed triangulated surface,” in *11th Pacific Conference on Computer Graphics and Applications* (Canmore, AB), 394–398.
- Hill, Y. R., Child, N., Hanson, B., Wallman, M., Coronel, R., Plank, G., et al. (2016). Investigating a novel activation-repolarisation time metric to predict localised vulnerability to reentry using computational modelling. *PLoS ONE* 11:e0149342. doi: 10.1371/journal.pone.0149342
- Hwang, M., Kwon, S.-S., Wi, J., Park, M., Lee, H.-S., Park, J.-S., et al. (2014). Virtual ablation for atrial fibrillation in personalized *in-silico* three-dimensional left atrial modeling: comparison with clinical catheter ablation. *Prog. Biophys. Mol. Biol.* 116, 40–47. doi: 10.1016/j.pbiomolbio.2014.09.006
- Jacquemet, V. (2010). The inverse problem of phase singularity distribution: an eikonal approach. *Comput. Cardiol.* 37, 863–866. doi: 10.1109/TBME.2010.2051156
- Jacquemet, V. (2016). Lessons from computer simulations of ablation of atrial fibrillation. *J. Physiol.* 594, 2417–2430. doi: 10.1113/JP271660
- Jacquemet, V., Virag, N., and Kappenberger, L. (2005). Wavelength and vulnerability to atrial fibrillation: Insights from a computer model of human atria. *Europace* 7(Suppl. 2), 83–92. doi: 10.1016/j.eupc.2005.03.017
- Jais, P., Sanders, P., Hsu, L.-F., Hocini, M., Sacher, F., Takahashi, Y., et al. (2006). Flutter localized to the anterior left atrium after catheter ablation of atrial fibrillation. *J. Cardiovasc. Electrophysiol.* 17, 279–285. doi: 10.1111/j.1540-8167.2005.00292.x
- Keener, J. P. (1991). An eikonal-curvature equation for action potential propagation in myocardium. *J. Math. Biol.* 29, 629–651.
- Kobza, R., Hindricks, G., Tanner, H., Schirdewahn, P., Dorszewski, A., Piorowski, C., et al. (2004). Late recurrent arrhythmias after ablation of atrial fibrillation: incidence, mechanisms, and treatment. *Heart Rhythm* 1, 676–683. doi: 10.1016/j.hrthm.2004.08.009
- Konukoglu, E., Relan, J., Cilingir, U., Menze, B. H., Chinchapatnam, P., Jadidi, A., et al. (2011). Efficient probabilistic model personalization integrating uncertainty on data and parameters: application to eikonal-diffusion models in cardiac electrophysiology. *Prog. Biophys. Mol. Biol.* 107, 134–146. doi: 10.1016/j.pbiomolbio.2011.07.002
- Krogh-Madsen, T., and Christini, D. J. (2012). Nonlinear dynamics in cardiology. *Annu. Rev. Biomed. Eng.* 14, 179–203. doi: 10.1146/annurev-bioeng-071811-150106
- Krueger, M. W., Dorn, A., Keller, D. U. J., Holmqvist, F., Carlson, J., Platonov, P. G., et al. (2013). *In-silico* modeling of atrial repolarization in normal and atrial fibrillation remodeled state. *Med. Biol. Eng. Comput.* 51, 1105–1119. doi: 10.1007/s11517-013-1090-1
- Labarthe, S., Bayer, J., Coudière, Y., Henry, J., Cochet, H., Jais, P., et al. (2014). A bilayer model of human atria: mathematical background, construction, and assessment. *EP Europace* 16(Suppl\_4), iv21–iv29. doi: 10.1093/europace/euu256
- Latcu, D. G., and Saoudi, N. (2014). How fast does the electrical impulse travel within the myocardium? the need for a new clinical electrophysiology tool: the conduction velocity mapping. *J. Cardiovasc. Electrophysiol.* 25, 395–397. doi: 10.1111/jce.12350
- Lee, Y., and Lee, S. (2002). Geometric snakes for triangular meshes. *Comput. Graphics Forum* 21, 229–238. doi: 10.1111/1467-8659.t01-1-00582
- Lee, Y., Lee, S., Shamir, A., Cohen-Or, D., and Seidel, H.-P. (2004). “Intelligent mesh scissoring using 3D snakes,” in *12th Pacific Conference on Computer Graphics and Applications* (Seoul), 279–287.
- Liang, J. J., Elafros, M. A., Chik, W. W., Santangeli, P., Zado, E. S., Frankel, D. S., et al. (2015). Early recurrence of atrial arrhythmias following pulmonary vein antral isolation: timing and frequency of early recurrences predicts long-term ablation success. *Heart Rhythm* 12, 2461–2468. doi: 10.1016/j.hrthm.2015.07.015
- Lines, G. T., MacLachlan, M. C., Linge, S., and Tveito, A. (2009). Synchronizing computer simulations with measurement data for a case of atrial flutter. *Ann. Biomed. Eng.* 37, 1287–1293. doi: 10.1007/s10439-009-9692-3
- Loewe, A. (2016). *Modeling Human Atrial Patho-electrophysiology From Ion Channels to ECG: Substrates, Pharmacology, Vulnerability, and P-waves*. PhD thesis, Karlsruhe Institute of Technology (KIT).
- Loewe, A., Krueger, M. W., Platonov, P. G., Holmqvist, F., Dössel, O., and Seemann, G. (2015). “Left and right atrial contribution to the p-wave in realistic computational models,” in *Functional Imaging and Modeling of the Heart 2015, Lecture Notes in Computer Science*, Vol. 9126 (Berlin; Heidelberg), 439–447.
- Loewe, A., Lutz, Y., Wilhelms, M., Sinnecker, D., Barthel, P., Scholz, E. P., Dössel, O., Schmidt, G., and Seemann, G. (2014a). *In-silico* assessment of the dynamic effects of amiodarone and dronedarone on human atrial patho-electrophysiology. *Europace* 16(Suppl. 4), iv30–iv38. doi: 10.1093/europace/euu230
- Loewe, A., Wilhelms, M., Dössel, O., and Seemann, G. (2014b). Influence of chronic atrial fibrillation induced remodeling in a computational electrophysiological model. *Biomed. Tech.* 59, S929–S932. doi: 10.1515/bmt-2014-5012
- Loewe, A., Wilhelms, M., Fischer, F., Scholz, E. P., Dössel, O., and Seemann, G. (2014c). Arrhythmic potency of human ether-a-go-go-related gene mutations L532P and N588K in a computational model of human atrial myocytes. *Europace* 16, 435–443. doi: 10.1093/europace/eut375
- Matene, E., and Jacquemet, V. (2012). Fully automated initiation of simulated episodes of atrial arrhythmias. *Europace* 14(Suppl. 5), v17–v24. doi: 10.1093/europace/eus271
- McDowell, K. S., Zahid, S., Vadakkumpadan, F., Blauer, J., MacLeod, R. S., and Trayanova, N. A. (2015). Virtual electrophysiological study of atrial fibrillation in fibrotic remodeling. *PLoS ONE* 10:e0117110. doi: 10.1371/journal.pone.0117110
- Mesas, C. E., Pappone, C., Lang, C. C., Gugliotta, F., Tomita, T., Vicedomini, G., et al. (2004). Left atrial tachycardia after circumferential pulmonary vein ablation for atrial fibrillation: electroanatomic characterization and treatment. *J. Am. Coll. Cardiol.* 44, 1071–1079. doi: 10.1016/j.jacc.2004.05.072
- Neic, A., Campos, F. O., Prassl, A. J., Niederer, S. A., Bishop, M. J., Vigmond, E. J., et al. (2017). Efficient computation of electrograms and ECGs in human whole heart simulations using a reaction-eikonal model. *J. Comput. Phys.* 346, 191–211. doi: 10.1016/j.jcp.2017.06.020
- Niederer, S. A., Kerfoot, E., Benson, A. P., Bernabeu, M. O., Bernus, O., Bradley, C., et al. (2011). Verification of cardiac tissue electrophysiology simulators using

- an n-version benchmark. *Philos. Trans. R. Soc. A Math. Phys. Eng. Sci.* 369, 4331–4351. doi: 10.1098/rsta.2011.0139
- Patel, A. M., d'Avila, A., Neuzil, P., Kim, S. J., Mela, T., Singh, J. P., et al. (2008). Atrial tachycardia after ablation of persistent atrial fibrillation: identification of the critical isthmus with a combination of multielectrode activation mapping and targeted entrainment mapping. *Circ. Arrhythm. Electrophysiol.* 1, 14–22. doi: 10.1161/CIRCEP.107.748160.
- Pernod, E., Sermesant, M., Konukoglu, E., Relan, J., Delingette, H., and Ayache, N. (2011). A multi-front eikonal model of cardiac electrophysiology for interactive simulation of radio-frequency ablation. *Comput. Graph.* 35, 431–440. doi: 10.1016/j.cag.2011.01.008
- Pezzuto, S., Kal'avský, P., Potse, M., Prinzen, F. W., Auricchio, A., and Krause, R. (2017). Evaluation of a rapid anisotropic model for ecg simulation. *Front. Physiol.* 8:265. doi: 10.3389/fphys.2017.00265
- Reumann, M., Bohnert, J., Seemann, G., Osswald, B., and Dössel, O. (2008). Preventive ablation strategies in a biophysical model of atrial fibrillation based on realistic anatomical data. *IEEE Trans. Biomed. Eng.* 55, 399–406. doi: 10.1109/TBME.2007.912672
- Sermesant, M., Coudiere, Y., Moreau-Villeger, V., Rhode, K. S., Hill, D. L. G., and Razavi, R. S. (2005). “A fast-marching approach to cardiac electrophysiology simulation for XMR interventional imaging,” in *MICCAI International Conference on Medical Image Computing and Computer-Assisted Intervention* (Berlin; Heidelberg), 607–615.
- Sermesant, M., Konukoglu, E., Delingette, H., Coudiere, Y., Chinchapatnam, P., Rhode, K., et al. (2007). “An anisotropic multi-front fast marching method for real-time simulation of cardiac electrophysiology,” in *Functional Imaging and Modeling of the Heart 2015, Lecture Notes in Computer Science*, volume 4466, pages 160–169.
- Sethian, J. A. (1996). A fast marching level set method for monotonically advancing fronts. *Proc. Natl. Acad. Sci. U.S.A.* 93, 1591–1595.
- Sethian, J. A. (1999). *Level Set Methods and Fast Marching Methods*. Cambridge, UK: Cambridge University Press.
- Sethian, J. A., and Vladimirov, A. (2000). Fast methods for the Eikonal and related Hamilton-Jacobi equations on unstructured meshes. *Proc. Natl. Acad. Sci. U.S.A.* 97, 5699–5703. doi: 10.1073/pnas.090060097
- Sethian, J. A., and Vladimirov, A. (2003). Ordered upwind methods for static Hamilton-Jacobi equations: Theory and algorithms. *SIAM J. Numer. Anal.* 41, 325–363. doi: 10.1137/S0036142901392742
- Trächtler, J. T., O., Loewe, A., Poremba, E., Luik, A., Schmitt, C., and Dössel, O. (2015). Virtualizing clinical cases of atrial flutter in a fast marching simulation including conduction velocity and ablation scars. *Curr. Dir. Biomed. Eng.* 1, 405–408. doi: 10.1515/cdbme-2015-0098
- Unger, L., Oesterlein, T., Seemann, G., Dössel, O., Spector, P., and Loewe, A. (2017). Estimating refractory periods during atrial fibrillation based on electrogram cycle lengths in a heterogeneous simulation setup. *Curr. Dir. Biomed. Eng.* 3, 317–320. doi: 10.1515/cdbme-2017-0181
- van Dam, P. M., Oostendorp, T. F., and van Oosterom, A. (2009). Application of the fastest route algorithm in the interactive simulation of the effect of local ischemia on the ECG. *Med. Biol. Eng. Comput.* 47, 11–20. doi: 10.1007/s11517-008-0391-2
- van Dam, P. M., and van Oosterom, A. (2003). Atrial excitation assuming uniform propagation. *J. Cardiovasc. Electrophysiol.* 14(10 Suppl.), S166–S171. doi: 10.1046/j.1540.8167.90307.x
- Verma, B., Oesterlein, T., Loewe, A., Luik, A., Schmitt, C., and Dössel, O. (2018). Regional conduction velocity calculation from clinical multichannel electrograms in human atria. *Comput. Biol. Med.* 92, 188–196. doi: 10.1016/j.compbiomed.2017.11.017
- Villacastín, J., Perez-Castellano, N., Moreno, J., and Gonzalez, R. (2003). Left atrial flutter after radiofrequency catheter ablation of focal atrial fibrillation. *J. Cardiovasc. Electrophysiol.* 14, 417–421. doi: 10.1046/j.1540-8167.2003.02418.x
- Wachter, A., Loewe, A., Krueger, M. W., Dössel, O., and Seemann, G. (2015). Mesh structure-independent modeling of patient-specific atrial fiber orientation. *Curr. Dir. Biomed. Eng.* 1, 409–412. doi: 10.1515/cdbme-2015-0099
- Waldo, A. L., and Feld, G. K. (2008). Inter-relationships of atrial fibrillation and atrial flutter: mechanisms and clinical implications. *J. Am. Coll. Cardiol.* 51, 779–786. doi: 10.1016/j.jacc.2007.08.066
- Wallman, M., Bueno-Orovio, A., and Rodriguez, B. (2013). “Computational probabilistic quantification of pro-arrhythmic risk from scar and left-to-right heterogeneity in the human ventricles,” in *Computing in Cardiology Conference (CinC)* (Zaragoza), 711–714.
- Wallman, M., Smith, N. P., and Rodriguez, B. (2012). A comparative study of graph-based, eikonal, and monodomain simulations for the estimation of cardiac activation times. *IEEE Trans. Biomed. Eng.* 59, 1739–1748. doi: 10.1109/TBME.2012.2193398
- Weber, F. M., Luik, A., Schilling, C., Seemann, G., Krueger, M. W., Lorenz, C., et al. (2011). Conduction velocity restitution of the human atrium—an efficient measurement protocol for clinical electrophysiological studies. *IEEE Trans. Biomed. Eng.* 58, 2648–2655. doi: 10.1109/TBME.2011.2160453
- Weber, F. M., Schilling, C., Seemann, G., Luik, A., Schmitt, C., Lorenz, C., et al. (2010). Wave-direction and conduction-velocity analysis from intracardiac electrograms—a single-shot technique. *IEEE Trans. Biomed. Eng.* 57, 2394–2401. doi: 10.1109/TBME.2010.2055056
- Wilhelms, M., Hettmann, H., Maleckar, M. M. C., Koivumäki, J. T., Dössel, O., and Seemann, G. (2013). Benchmarking electrophysiological models of human atrial myocytes. *Front. Physiol.* 3:487. doi: 10.3389/fphys.2012.00487
- Yamada, T., and Kay, G. N. (2013). Atrial flutter following pulmonary vein isolation: what is the mechanism? *J. Cardiovasc. Electrophysiol.* 24, 1186–1188. doi: 10.1111/jce.12167
- Zahid, S., Whyte, K. N., Schwarz, E. L., Blake, R. C., Boyle, P. M., Chrispin, J., et al. (2016). Feasibility of using patient-specific models and the “minimum cut” algorithm to predict optimal ablation targets for left atrial flutter. *Heart Rhythm* 13, 1687–1698. doi: 10.1016/j.hrthm.2016.04.009
- Zhao, J., Kharche, S. R., Hansen, B. J., Csepe, T. A., Wang, Y., Stiles, M. K., et al. (2015). Optimization of catheter ablation of atrial fibrillation: insights gained from clinically-derived computer models. *Int. J. Mol. Sci.* 16, 10834–10854. doi: 10.3390/ijms160510834

**Conflict of Interest Statement:** The authors declare that the research was conducted in the absence of any commercial or financial relationships that could be construed as a potential conflict of interest.

Copyright © 2019 Loewe, Poremba, Oesterlein, Luik, Schmitt, Seemann and Dössel. This is an open-access article distributed under the terms of the Creative Commons Attribution License (CC BY). The use, distribution or reproduction in other forums is permitted, provided the original author(s) and the copyright owner(s) are credited and that the original publication in this journal is cited, in accordance with accepted academic practice. No use, distribution or reproduction is permitted which does not comply with these terms.